시야 제약 환경에서 초소형 무인항공기의 실시간 가시성 기반 경로계획

Real-time Visibility-aware Planning for Micro Aerial Vehicles under Limited Field of View and Occlusion Constraints

초록

초소형 무인항공기는 작은 크기, 군집 운용, 경제성 등으로 산업·재난·점검 등 다양한 분야에서 잠재력이 크지만, 센서와 연산 자원 제약으로 활용이 제한적이다. 비전센서 기반 운용이 보편화되면 활용도는 크게 높아질 것이나, 이를 위해 제한된 시야각과 장애물로 인한 가림 등 복합 제약 속에서도 목표물 가시성을 유지해야 한다. 복합 제약을 해결하기 위한 기존 최적화 기반 기법은 초소형 항공기의 연산환경에서 실시간 운용이 어렵다. 본 연구는 제한된 연산환경에서도 가시성 유지와 가림 회피를 보장하는 경량 경로 계획·제어 기법을 제안하며, 이는 다중 목표물 시나리오로도 확장이 가능하다. 제안 기법은 목표물 가시성 보장을 통해 작업 효율과 안전성을 높일 수 있으며, 시뮬레이션과 쿼드로터 실험을 통해 이를 확인하였다.

Key Words : Micro Aerial Vehicle, Vision-based Planning, Optimization-free Control

Introduction

Micro aerial vehicles (MAVs) have significant potential in industrial inspection, disaster response, infrastructure monitoring, and other mission-critical applications due to their small size, maneuverability, and low deployment cost. However, in practice, their deployment remains limited because lightweight onboard systems impose both sensing and computational constraints, preventing sustained and reliable operation in complex environments. Integrating vision sensors into MAVs can unlock far broader industrial applications—ranging from target detection[1] to multirotor perching[2] and powerline inspection[3]—yet this also introduces strict visibility requirements that are challenging to meet in real time. These limitations are further compounded by the high computational demands of conventional optimization-based methods. This work presents a computationally efficient planning and control framework that ensures target visibility under limited field of view and occlusion constraints, enabling broader, safer, and more reliable use of vision-based MAVs in demanding real-world missions.

Maintaining target visibility in MAV operations is challenging for several reasons. First, the limited field of view of the camera constrains the allowable relative orientation between the MAV and the target. Second, occlusions caused by obstacles further restrict visibility to regions where a clear line of sight can be maintained. Third, fixed sensor placement on the vehicle together with bounded actuation introduces additional kinematic and control input limitations. A common design choice to address these challenges is optimization-based trajectory planning, such as model predictive control (MPC)[4,5]. Recent advances in lightweight cameras and embedded processors have enabled the integration of onboard perception systems into MAV platforms. However, these platforms operate under strict constraints on computational resources, payload capacity, and energy usage, making optimization intensive planning methods, particularly those involving nonconvex MPC formulations, impractical for real-time execution. These limitations motivate the need for computationally efficient, optimization-free control strategies that can still guarantee the satisfaction of vision-based constraints during dynamic maneuvers.

In this work, we present an optimization-free planning and control framework specifically designed for MAVs that operate under vision-based constraints. The proposed method enforces visibility through a feedback control law that can run in real-time without heavy computation but with lightweight matrix operations. The framework handles both limited field of view and occlusion constraints while guaranteeing feasibility and convergence to any admissible target configuration. The approach is first developed for a single target scenario and then extended to maintain visibility of multiple targets

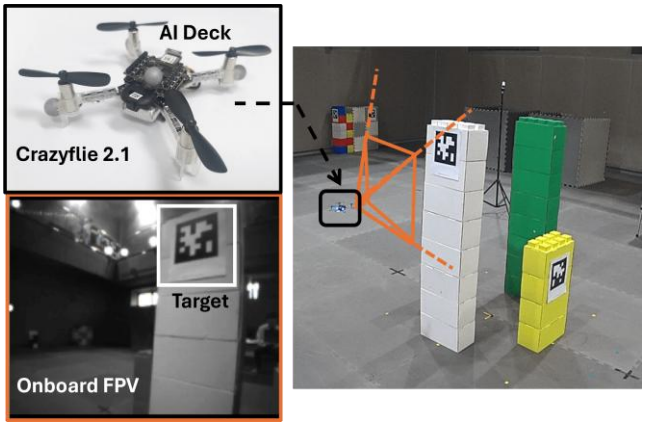

Fig. 1. Snapshot of the camera-equipped nano quadrotor in flight, highlighting the target of interest within the field of view (orange). The hardware setup includes a Crazyflie quadrotor with an AI deck capturing greyscale images.

simultaneously.

The main contributions of this work are as follows:

- Development of a lightweight feedback-based motion planning framework for MAVs that ensures target visibility under both limited field of view and occlusion constraints without any online optimization.
- Provision of formal guarantees for feasibility and convergence for any admissible initial and goal configurations.
- Extension of the visibility aware control law from a single target setting to multiple targets, enabling persistent observation of all specified targets.
- Validation of the proposed framework is conducted through numerical simulations and hardware experiments on a quadrotor platform, as shown in Fig. 1, demonstrating its suitability for real-time MAV operations.

Related Work

Visibility constrained control for mobile robots has been pursued mainly through optimization-based planning and feedback motion planning. In optimization-based approaches, MPC and trajectory optimization encode field of view and occlusion constraints either as hard state constraints or as penalties in the cost, for camera kinematics[6] and multirotor dynamics[4,7], with soft penalties to mitigate occlusions[8] and image plane projections that keep features outside obstacle projections via convex programs[9]. While effective in structured scenarios, these methods often require solving nonconvex programs online, which limits recursive feasibility, goal convergence, and practicality on MAV platforms. Recently, additional control barrier functions (CBF) have also been used as safety filters that adjust inputs to keep the state in target visible sets[10,11,12], but CBF based filters alone typically do not provide a complete planning mechanism with guarantees of convergence under visibility constraints. Trajectory optimization has also produced visibility preserving paths using optimality principles or online programs that maximize landmark visibility[13,14,15], but these approaches commonly rely on precomputed motion primitives or offline-computed trajectories.

Sensor based feedback motion planning generates continuous trajectories from a feedback policy within the dynamical systems framework[16], enabling online use of state information and robustness that open-loop planners lack[17]. Classical artificial potential fields are simple but suffer from local minima[18], while navigation functions and harmonic potentials recover convergence under stronger assumptions[16,19]. Practical variants integrate onboard sensing for dynamic settings with 2D LiDAR and

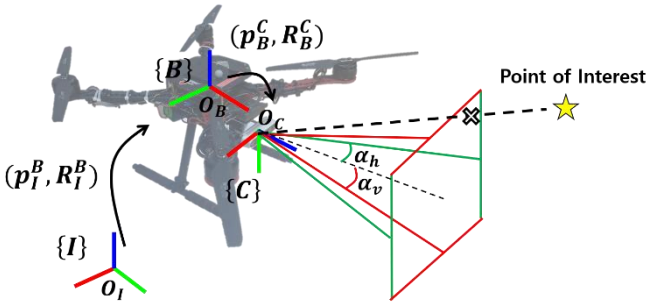

Fig. 2. Diagram of the camera-equipped multirotor illustrating the reference frames, camera field-of-view, and the point-of-interest.

moving obstacles[20,21,22], and use partial visual cues to enhance collision avoidance[23]. Yet most feedback planners assume omnidirectional sensing and do not explicitly encode directional vision constraints such as field of view limits and occlusions. Our previous work[24] designed a reference governor that modifies the reference to satisfy field of view constraints under a closed loop system, but it does not handle occlusions and does not guarantee convergence. These limitations motivate our optimization-free feedback motion planning framework, which enforces visibility constraints while remaining suitable for real-time execution and providing feasibility and convergence guarantees.

Problem Statement

We consider the motion planning problem for a MAV equipped with a vision sensor with limited FoV. The system is modeled as a single integrator:

$$\dot{\mathbf{y}} = \mathbf{w} \tag{1}$$

where $y = [p^T, \psi]^T \in \mathcal{C} = \mathbb{R}^3 \times \mathbb{S}^1$ is the configuration of the MAV, with $\mathbf{p} \in \mathbb{R}^3$ representing its position and $\psi \in \mathbb{S}^1$ its yaw angle. The control input is given by $\mathbf{w} = [\mathbf{v}^T, \omega]^T \in \mathbb{R}^4$, where $\mathbf{v} \in \mathbb{R}^3$ is the linear velocity and $\omega \in \mathbb{R}$ is the angular velocity in the yaw direction. The control input $\mathbf{w}$ is subject to box constraints: $|w_i| \leq \bar{w}_i, i = 1, \cdots, 4$ The use of the yaw angle as the attitude representation, rather than a full SO(3) orientation, is motivated by its practical usage in utilizing the differential flatness of MAV[25]. The workspace $\mathcal{W} \subset \mathbb{R}^3$, is a bounded, compact, convex set containing known obstacles $\mathcal{O}_1, \cdots, \mathcal{O}_{n_o} \subset \mathcal{W}$, each modeled as closed. The point-of-interest (PoI), denoted by $\mathbf{p}^l \in \mathbb{R}^3$, lies strictly outside the interiors of all obstacles, i.e., $\mathbf{p}^l \in \text{int}(\mathcal{W}) \backslash \cup_{i=1}^{n_o} \text{int}(\mathcal{O}_i)$, where $\text{int}(\cdot)$ denotes the interior of the set.

We adopt a pinhole camera as the sensor model with extrinsic parameters R_B^C, and $\mathbf{p}_B^C$. Note that the subscripts and superscripts I, B, C denote the inertial, body, and camera frames, respectively. The position of the PoI in the camera frame, $\mathbf{p}_C^l = [x_C^l \quad y_C^l \quad z_C^l]^T$, is given by

$$\mathbf{p}_C^l = R_B^{C,T}\left(R_I^{B,T}(\mathbf{p}_I^l - \mathbf{p}_I^B) - \mathbf{p}_B^C\right) \tag{2}$$

For simplicity, we assume that the camera is rigidly mounted to the robot's body frame and located at the center of mass, i.e., $\mathbf{p}_B^C = \mathbf{0}$. Additionally, the camera is assumed to be forward-facing, meaning its optical axis is aligned with the robot's heading direction. The camera has pyramidal shaped FoV, as illustrated in Fig. 2, with half-angles $\alpha_h, \alpha_v \in (0, \pi/2)$.

The position of the PoI in camera frame $\mathbf{p}_C^l$ is required to lie within the FoV of the camera to remain visible. The limited FoV constraints for the horizontal and vertical FoV can be expressed as:

$$\left|x_C^l / z_C^l\right| \leq \tan \alpha_h, \tag{3}$$

$$\left|y_C^l / z_C^l\right| \leq \tan \alpha_v, \tag{4}$$

$$z_C^l > 0, \tag{5}$$

where (3) and (4) ensure that the PoI remains within the horizontal and vertical FoV, respectively. Constraint (5) ensures that the PoI lies in front of the camera.

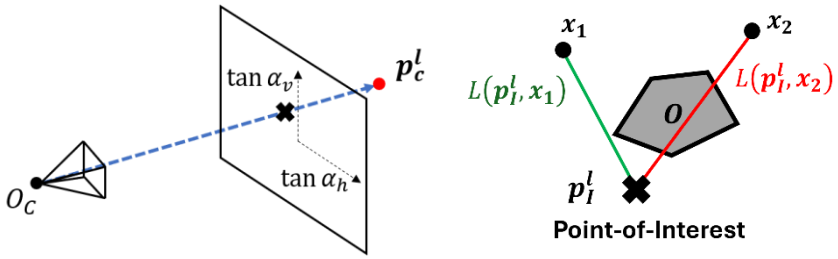

Fig. 3. The diagrams illustrate (left) the field-of-view constraints, showing the horizontal FoV α_h and vertical FoV α_v, and (right) the characterization of occlusion constraints based on the line-of-sight between the PoI and the current state.

Occlusion by the obstacles might cause loss of the visibility of the PoI. Occlusion occurs when the Line-of-Sight (LoS) from the camera to the PoI intersects an obstacle. This condition can be formulated as

$$L(\mathbf{p}^l, \mathbf{p}) \cap \mathcal{O}_i = \emptyset, i = 1, \cdots, n_o \tag{6}$$

where $L(\mathbf{p}^l, \mathbf{p})$ is the line between the PoI and the robot position, $L(\mathbf{p}^l, \mathbf{p}) = \{(1-\gamma)\mathbf{p}^l + \gamma\mathbf{p} : \gamma \in [0,1]\}$. The limited field of view and occlusion constraints are illustrated in Fig. 3.

The objective is to design a control vector field (CVF) $\mathbf{g}: \mathcal{C} \times \mathcal{C} \to \mathbb{R}^4$, which defines a feedback policy $\mathbf{w} = \mathbf{g}(\mathbf{y}, \mathbf{y}_g)$ that satisfies both the visibility and input constraints while ensuring convergence to the given goal $\mathbf{y}_g \in \mathcal{C}_a \subset \mathcal{C}$. where $\mathcal{C}_a$ is the admissible subset of the configuration space.

Visibility-Guaranteed Motion Planning with Limited Field of View

We begin by designing a control policy $\mathbf{g}_q: \mathcal{C}_q \times \mathcal{C}_q \to \mathbb{R}^3$ for a 3-dimensional pose $\mathbf{y}_q = [x, y, \psi]^T$ and goal $\mathbf{y}_{g,q} = [x_g, y_g, \psi_g]^T$, where the configuration space is $\mathcal{C}_q = \mathbb{R}^2 \times \mathbb{S}^1$. This formulation focuses on handling the horizontal FoV constraints for a single PoI $\mathbf{p}_I^l$. We then extend the policy $\mathbf{g}$ to the full state space to incorporate vertical FoV constraints.

Horizontal FoV Constraints

The naive attraction field $\mathbf{g}_{a,q} = \mathbf{y}_{g,q} - \mathbf{y}_q$ can produce non-converging trajectories or local attractors because the admissible set under the horizontal FoV constraint $A = \{\mathbf{y}_q : |x_C^l / z_C^l| \le \tan\alpha_h, z_C^l > 0\}$ is non-convex. To ensure convergence, we first build a convex set Q that is locally diffeomorphic to A, allowing a simple attraction field on Q. Repulsive potential is also added near the boundary of A to maintain feasibility.

We define a local set $\mathcal{C}_{S,q} = \mathbb{R}^2 \times [\psi_r - \pi, \psi_r + \pi] \subset \mathcal{C}_q$, with reference yaw ψ_r, and the local admissible

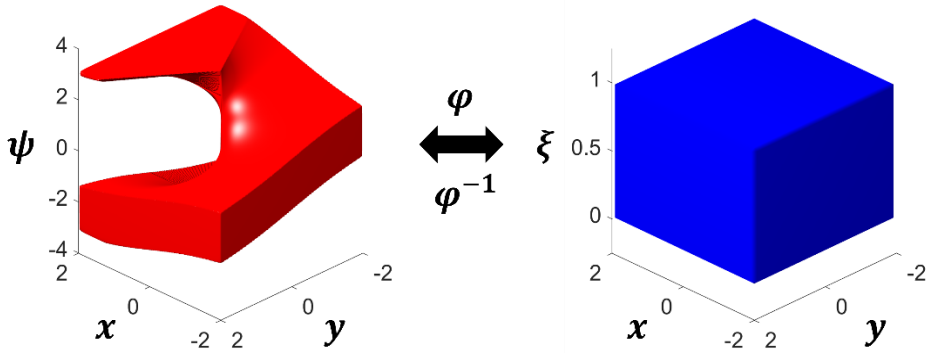

Fig. 4. Diagram illustrating the diffeomorphism φ mapping the admissible set of horizontal FoV constraints A to the corresponding convex set Q.

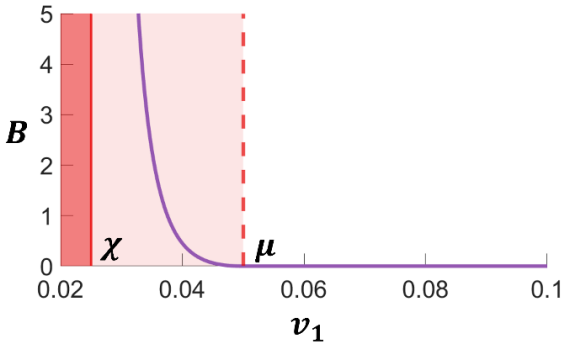

Fig. 5. Graph of the barrier function $B(\xi_1, \xi_2, \mu, \chi)$ with respect to ξ_1 when $\xi_2 = 0$, $\chi = 0.025$, and $\mu = 0.05$.

set as $A_S \subset A$. Due to the 2π–periodicity of $\mathbb{S}^1$, any state can be mapped into A_S. Following Cotorruelo et al.[26], we construct a diffeomorphism $\varphi: A_S \to Q = \text{int}\, A_{S,p} \times [0,1]$ where $A_{S,p} = \text{proj}_{\mathbb{R}^2} A_S$ is the projection of A_S onto the position subspace.

For $\mathbf{y}_q \in A_S$,

$$\varphi(\mathbf{y}_q) = [x, y, \xi]^T, \qquad \xi = \frac{\psi - \underline{f}(x,y)}{\overline{f}(x,y) - \underline{f}(x,y)} \in [0,1] \tag{7}$$

and $\overline{f}(x,y)$ and $\underline{f}(x,y)$ are the upper and lower yaw bounds satisfying the FoV constraint. These bounds are

$$\overline{f}(x,y), \underline{f}(x,y) = \text{atan2}(y - y^l, x - x^l) \pm \alpha_h. \tag{8}$$

The admissible set A_S and its convex counterpart Q are graphically illustrated in Fig. 4. We define an attraction field in the transformed coordinates and map it back via the local diffeomorphism φ, yielding

$$f_{a,q}(\mathbf{y}_q, \mathbf{y}_{g,q}) = -k\left(\varphi(\mathbf{y}_{g,q}) - \varphi(\mathbf{y}_q)\right) \tag{9}$$

for $\mathbf{y}_{g,q} \in A_S$. The convexity of Q and smoothness of φ ensure convergence to admissible goal $\mathbf{y}_{g,q}$.

To prevent constraint violation in the converging trajectory, we define a repulsive field. The barrier function $B(\xi_1, \xi_2, \mu, \chi)$ with scalars $\mu > \chi > 0$ is defined as:

$$B(\xi_1, \xi_2, \mu, \chi) = \left[\min\left\{0, \frac{(\xi_1 - \xi_2 + 1)^2 - (\mu + 1)^2}{(\xi_1 - \xi_2 + 1)^2 - (\chi + 1)^2}\right\}\right]^2 \tag{10}$$

Induces repulsion when $\xi_1 > \xi_2$, as shown in Fig. 5. Within Q ($\xi \in [0,1]$), the repulsive potential is

$$P_r(\xi) = B(\xi, 0, \mu, \chi) + B(1, \xi, \mu, \chi) \tag{11}$$

And the corresponding repulsive field is

$$f_{r,q}(\xi) = -\nabla P_r = \left[0 \quad 0 \quad -\frac{\partial P_r}{\partial \xi}\right]^T. \tag{12}$$

The complete CVF combines attraction and repulsion in the yaw component:

$$g_q(y_q, y_{g,q}) = \frac{1}{\eta} H_q \left(\nabla\varphi(y_q)\right)^{-1} (f_{a,q} + f_{r,q}), \tag{13}$$

where $\eta = \left\|(\nabla\varphi)^{-1}(f_{a,q} + f_{r,q})\right\|_\infty$ is a normalizing coefficient, and $H_q = \text{diag}(\overline{w}_x, \overline{w}_y, \overline{w}_\psi) > 0$ is a positive diagonal matrix that enforces the input constraints.

A related numerical example is shown in Fig. 6, where the proposed CVF maintains convergence to

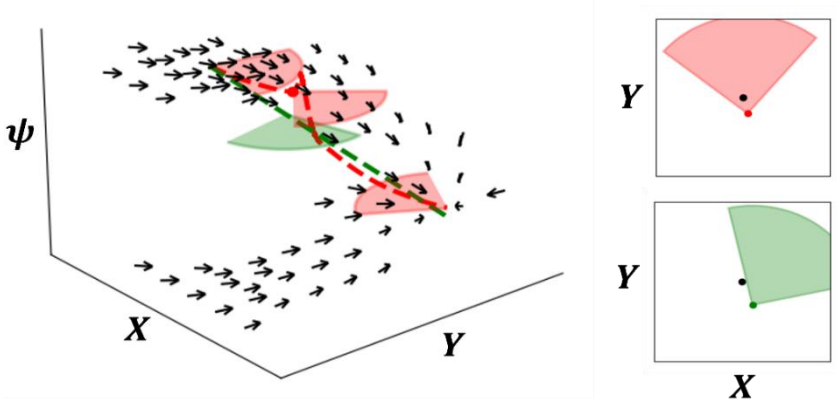

Fig. 6. (Left) For a horizontal FoV of $\alpha_h = 45°$, trajectories generated by the proposed planner (red) and by using only the attraction field (green) are compared. The vector field corresponding to the proposed planner is also shown. (Right) An instance where using only the attraction field leads to a violation, whereas the proposed planner maintains continuous visibility of the PoI (black dot).

the goal via the diffeomorphic modulation and satisfies the FoV constraints through the repulsive potential, whereas the naive attraction field violates these constraints.

Vertical FoV Constraints

Extending the horizontal FoV CVF in (13) to the full configuration space, we design $\mathbf{g}: \mathcal{C} \times \mathcal{C} \to \mathbb{R}^4$ to also satisfy the vertical FoV constraints (4). The diffeomorphism-based approach from the previous section cannot be applied directly, since the vertical FoV limits break the assumptions required to construct the same local diffeomorphism φ. Instead, we add a control law for the z-coordinate that explicitly incorporates vertical FoV limits.

Let $\overline{z}(x,y,\psi)$ and $\underline{z}(x,y,\psi)$ as the maximum and minimum admissible z values, respectively, satisfy the vertical FoV constraint at a fixed configuration (x,y,ψ). By symmetry, $\overline{z}(x,y,\psi) = -\underline{z}(x,y,\psi)$. From the partial CVF (13), the desired direction vector toward the goal $\mathbf{y}_g$ is

$$\mathbf{d}_d(\mathbf{y},\mathbf{y}_g) = \begin{bmatrix} g_{x,q} & g_{y,q} & z_g - z & g_{\psi,q} \end{bmatrix}^T. \tag{14}$$

However, as illustrated in Fig. 7, directly following (15) may violate the vertical FoV constraints.

Since any (x,y,ψ) satisfying horizontal FoV constraints automatically admits some feasible z, and condition (5) prevents $z_C^l = 0$ at the PoI, there always exists a safe vertical direction toward $z = z^l$:

$$\mathbf{d}_s(\mathbf{y},\mathbf{y}_g) = [0 \quad 0 \quad z_I^l - z \quad 0]^T \tag{15}$$

When $z = \overline{z}$, following $\mathbf{d}_d$ is infeasible if $\angle(\mathbf{d}_d, \mathbf{d}_s) > \angle(\nabla\overline{z}|_{\mathbf{y}}, \mathbf{d}_s)$, where $\angle(\cdot,\cdot)$ denotes the angle between two vectors. To prevent such cases, we define a repulsive potential as:

$$\overline{P}_z = \overline{B}(\mathbf{y},\delta,\epsilon_z) \cdot HS\left(\angle(\mathbf{d}_d,\mathbf{d}_s) - \angle\left(\nabla\overline{z}|_{\mathbf{y}},\mathbf{d}_s\right)\right), \tag{16}$$

where $\overline{B}(y,\delta,\epsilon_z) = B(\overline{z},z,\delta,\epsilon_z)$, $\delta > \epsilon_z > 0$, and $HS(\cdot)$ is the Heaviside step function. $\underline{P}_z$ can be defined in the same way for the lower boundary $\underline{z}(x,y,\psi)$, and $P = \overline{P}_z - \underline{P}_z$, serves as an indicator of whether the current state is approaching an infeasible region.

- If $P = 0$, we follow $\mathbf{d}_d$.
- If $P > 0$ at the upper boundary, we replace the z-component with the directional derivative of $\overline{z}$ along $\mathbf{g}_q$ as $\overline{\mathbf{d}}_m(\mathbf{y},\mathbf{y}_g) = \begin{bmatrix} g_{x,q} & g_{y,q} & D_{g_q}\overline{z} & g_{\psi,q} \end{bmatrix}^T$.
- For the lower boundary, we similarly define $\underline{\mathbf{d}}_m$.

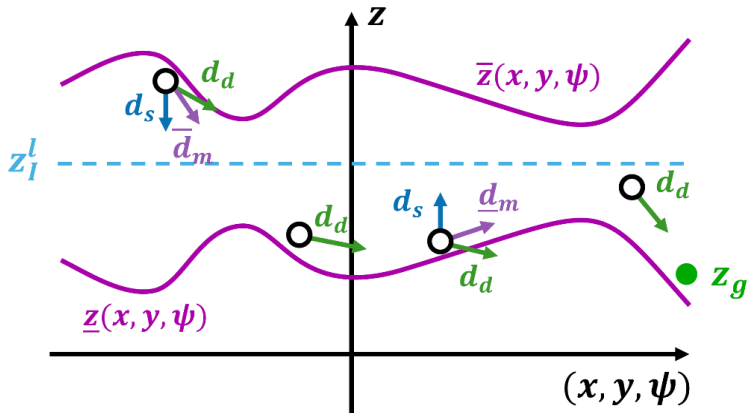

Fig. 7. Illustration of the z−coordinate control law design under vertical FoV constraints. If the desired control law $\boldsymbol{d_d}$, directed toward $\boldsymbol{z_g}$, remains within the vertical FoV bounds $[\overline{z}, \underline{z}]$, the control policy proceeds as intended. However, if there is a risk of exceeding these bounds, the directional derivative of the active boundary, $\bar{\boldsymbol{d}}_{\boldsymbol{m}}$ or $\underline{\boldsymbol{d}}_{\boldsymbol{m}}$, is applied to ensure feasibility.

- If $P = 0$ but $\overline{P} \neq 0$, we hold altitude as $d_z(y, y_g) = [g_{x,q}, g_{y,q}, 0, g_{\psi,q}]^T$.

The hybrid CVF is then

$$\mathbf{g}_u(\mathbf{y}, \mathbf{y}_g) = \begin{cases} \bar{\mathbf{d}}_m(\mathbf{y}, \mathbf{y}_g), & P > 0 \\ \underline{\mathbf{d}}_m(\mathbf{y}, \mathbf{y}_g), & P < 0 \\ \mathbf{d}_d(\mathbf{y}, \mathbf{y}_g), & P = \overline{P} = \underline{P} = 0 \\ \mathbf{d}_z(\mathbf{y}, \mathbf{y}_g), & \text{otherwise} \end{cases} \tag{17}$$

and is normalized to enforce input bounds:

$$\mathbf{g}(\mathbf{y}, \mathbf{y}_g) = \frac{1}{\eta_m} H \mathbf{g}_u(\mathbf{y}, \mathbf{y}_g) \tag{18}$$

where the normalization factor is defined as $\eta_m = \|g_u(y, y_g)\|_\infty$, and $H = \mathrm{diag}(\overline{w}_x, \overline{w}_y, \overline{w}_z, \overline{w}_\psi)$ is a diagonal scaling matrix.

Motion Planning for Occlusion Avoidance

While the CVF in (18) enforces limited FoV constraints, it does not prevent visibility loss from environmental occlusions. In obstacle-rich environments, the PoI may be hidden, violating the occlusion constraint (6). The key observation is that the **occlusion-free region** is **star-shaped**, enabling the use of modulation-based dynamical systems[27] to maintain visibility while navigating around occlusions.

From the line-of-sight condition (6), the occluded region of the PoI $\mathbf{p}^l$ by an obstacle O is

$$D(\mathbf{p}^l, O) = \{\mathbf{p} \in \mathbb{R}^3 : L(\mathbf{p}^l, \mathbf{p}) \cap O \neq \emptyset\}, \tag{20}$$

a closed set. For an obstacle set $\mathcal{O} = \{O_i\}_{i=1}^N$, the occlusion-free region is

$$S(\mathbf{p}^l, \mathcal{O}) = \mathcal{W} \backslash \cup_{i=1,\cdots,N} D(\mathbf{p}^l, O_i), \tag{21}$$

and the occlusion constraint requires $\mathbf{p} \in \mathrm{int}(S(\mathbf{p}^l, \mathcal{O}))$. Fig. 8 illustrates occlusion-free region of the polygonal environment. Since obstacles are subsets of the occluded region, satisfying the occlusion constraint also ensures collision avoidance.

Although the framework applies to general 3D obstacles, computing exact 3D visibility regions is computationally expensive. Thus, we focus on 2D projections—valid when the robot cannot fly over obstacles. In this setting, the occlusion-free region S can be computed efficiently using visibility algorithms [28, 29].

We then design a 2D CVF in the position space $\mathbf{y}_p = [x, y]^T$ using the modulation framework:

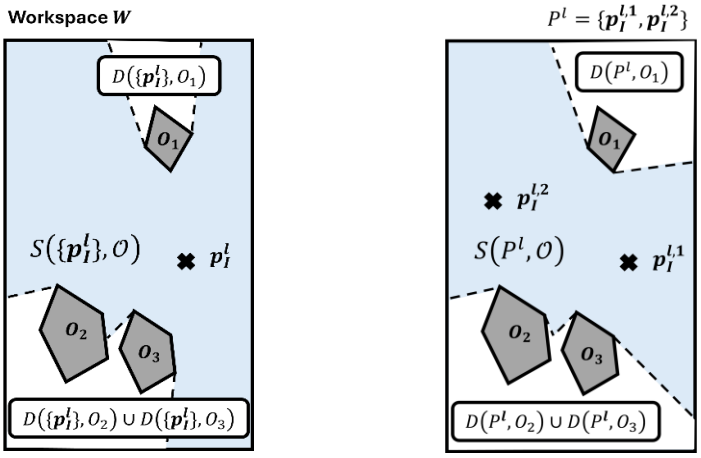

Fig. 8. Illustration of the occlusion constraint based on the line-of-sight and the occlusion-free region (blue area) from obstacles (grey area) for (left) a single PoI and (right) the two PoIs depicted in crosses.

$$\mathbf{g}_p(\mathbf{y}_p, \mathbf{y}_{g,p}) = N(\mathbf{y}_p, S) f_{a,p}(\mathbf{y}_p, \mathbf{y}_{g,p}), \tag{22}$$

where $N(\mathbf{y}_p, S)$ is the modulation matrix encoding the geometry of S.

Finally, to combine occlusion avoidance with FoV constraints, we update the CVF as

$$\mathbf{g}_q(\mathbf{y}_q, \mathbf{y}_{g,q}) = \frac{1}{\eta} H_q \left(\nabla\varphi(\mathbf{y}_q)\right)^{-1} \begin{bmatrix} N(\mathbf{y}_p, S) & 0 \\ 0 & 1 \end{bmatrix} (f_{a,q} + f_{r,q}). \tag{23}$$

where η normalizes the vector field and H_q enforces input bounds.

Theoretical Guarantee

The theoretical analysis below guarantees satisfaction with FoV constraints and occlusion constraints. It also guarantees convergence to the goal pose of the multirotor. We provide the theorem and proof sketch, and more detailed rigorous theoretical proof is given in the Appendix.

Theorem 1. (Feasibility & Convergence)

Consider the system dynamics in (1) under the control law given in Eq. (23). Assume the admissible set, defined by the limited FoV and occlusion-avoidance constraints, is nonempty at the initial time and the goal configuration lies strictly inside it. Then:

1) Feasibility (Forward Invariance): If the initial state is in the admissible set, the closed-loop trajectory remains inside the admissible set for all future time, ensuring that visibility and collision avoidance constraints are never violated.
2) Convergence: The system state asymptotically converges to the goal configuration while remaining inside the admissible set.

These properties are guaranteed without iterative optimization, enabling real-time implementation on resource-constrained MAV platforms.

Proof Sketch.

The horizontal FoV constraints are enforced by mapping the nonconvex yaw-admissible set to a convex domain via a fixed diffeomorphism and adding a barrier term, ensuring forward invariance in yaw. The vertical FoV constraints are maintained by switching between a nominal direction and a boundary-following mode, preserving invariance in altitude. Occlusion avoidance is guaranteed by modulating the planar attraction field with a star-shaped safe set, keeping the trajectory within the occlusion-free

region. The combined control law preserves each individual constraint, and a Lyapunov-like argument shows that the goal state in the admissible set is asymptotically reached. ■

Theorem 2. (Computational Complexity)

Consider the control law in Eq. (23) with a single PoI. Each update of Eq. (23)—including FoV bound evaluation, the diffeomorphism mapping φ, the fixed-size Jacobian inverse, and the remaining fixed-size vector/matrix operations (e.g., attractive term and normalization)—runs in

$$T_{update} = \Theta(1)$$

with $O(1)$ auxiliary memory. The constant factor consists of a small, fixed set of trigonometric evaluations, scalar arithmetic, and 3×3 / 2×2 matrix–vector operations.

Proof) For a single POI, and diffeomorphism mapping are computed with a fixed number of trigonometric and scalar operations; the Jacobian $\nabla\varphi(\mathbf{y}_q)$ is fixed size and inverted in constant time. The number of virtual-obstacle components is constant, and each modulation step involves only fixed-size matrix and vector operations. The remaining terms (f_a, f_r), block-diagonal multiplication, and normalization are also constant-time. Summing these gives

$$T_{update} = O(1) + O(1) + O(1) = \Theta(1),$$

with $O(1)$ auxiliary memory. Hence, the controller executes in constant time and memory for the single PoI case. ■

Extension to Multiple Points of Interest

The single-PoI visibility-constrained control framework can be extended to handle multiple targets $P^l = \{\mathbf{p}_1^l, \dots, \mathbf{p}_{n_L}^l\}$ by redefining the admissible yaw and pitch bounds so that they simultaneously satisfy the FoV limits for all PoIs.

For **horizontal FoV**, the lower bound is the maximum of all individual lower bounds, and the upper bound is the minimum of all individual upper bounds as

$$\overline{f} = \min_i\{\arctan2(y - y^{l,i}, x - x^{l,i}) + \alpha_h\}, \quad \underline{f} = \max_i\{\arctan2(y - y^{l,i}, x - x^{l,i}) - \alpha_h\}.$$

Where these bounds do not overlap, the intersection is empty, creating virtual obstacles — regions in which it is impossible to see all PoIs at once. These virtual obstacles typically form lens-shaped zones between PoIs and are added to the obstacle set for avoidance as in Fig. 9a.

For **vertical FoV**, a similar process is applied using upper and lower pitch bounds for each PoI, and the barrier function is extended as $P = \max_i \overline{P}_i - \max_i \underline{P}_i$. Conflicts between bounds from different PoIs also generate virtual obstacles, which are again incorporated into the avoidance map.

For **occlusion handling**, the occlusion-free region for multiple PoIs is the intersection of each individual occlusion-free region. If this region becomes fragmented or highly non-convex, a suitable star-shaped subset is constructed around the union of occluded areas and virtual obstacles. The controller then modulates the vector field to remain in this subset while moving toward the goal.

This approach allows the robot to satisfy FoV and occlusion constraints for all PoIs simultaneously, with virtual obstacles representing the key new element compared to the single-PoI case. And the graphical illustration of the virtual obstacles for multiple PoIs is given in Fig. 9.

Remark 1. (Application: PoI Transition)

The framework also supports online switching between PoIs while always keeping at least one visible. Unlike existing vision-based localization algorithms, which typically assume a predefined motion to maintain visibility of visual markers, our method explicitly enforces this condition, as illustrated in Fig. 10. This is done by ensuring there is an intermediate region where two PoIs are simultaneously visible and not occluded. We compute the union of occluded regions for each PoI, add the multiple-PoI virtual obstacles, and then select a waypoint within the remaining feasible space that maintains visibility of

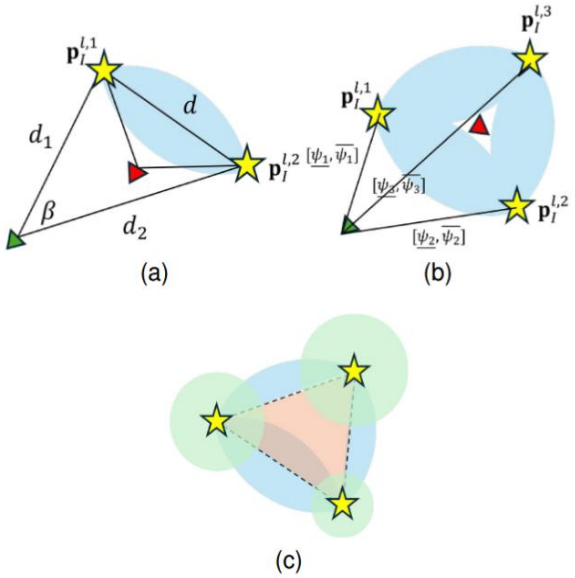

Fig. 9. Virtual obstacles (blue) for (a) horizontal FoV constraints with two PoIs (yellow stars) and (b) with three PoIs. (c) Total obstacle set for three PoIs: intersection of horizontal FoV obstacles, vertical FoV obstacles (green circles), and the PoI convex hull (orange).

both PoIs. The robot navigates to this waypoint, transitions its focus to the second PoI once inside, and then proceeds toward the final goal—guaranteeing continuous visibility throughout the switch.

Remark 2. (Computational Complexity for Multiple PoI Case)

If the number of points of interest increases to $n_L > 1$, the computation of the FoV bounds requires a pass over all PoIs, and the number of virtual-obstacle components K can grow with n_L. In the worst case, the horizontal FoV construction generates $O(n_L^2)$ pairwise virtual obstacles, while vertical FoV components can be pruned to $O(n_L)$. These yields

$$T_{update} = \Theta(n_L + n_L^2) = \Theta(n_L^2)$$

in the worst-case scenario. Thus, while the single-POI case achieves constant-time computation, the multiple-POI case reaches quadratic scaling.

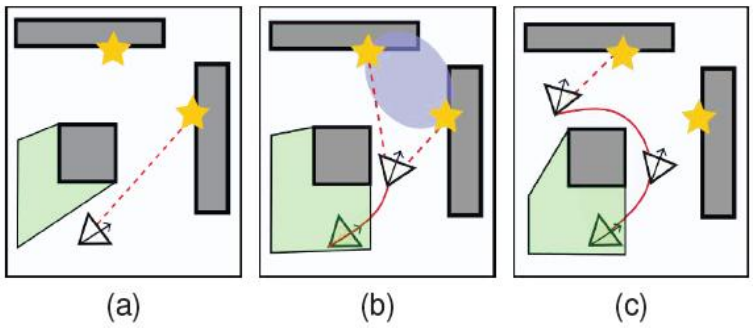

Fig. 10. Dynamic PoI switching during navigation. The PoI (yellow star), occluded regions (green), and obstacles (grey) are shown. (a) The trajectory is planned via the first PoI. (b) Upon entering a region where both PoIs are visible, a virtual obstacle (blue ellipse) is added. (c) After ensuring visibility of the second PoI, the first is removed, and it maintains visibility of the second.

Evaluation

Simulation

In a 2D environment with one obstacle and one PoI (Fig. 11), we evaluated the proposed method under horizontal FoV and occlusion constraints, comparing it to two baselines. The first, by Hayet et al.[31], also handles occlusion and limited FoV using a Generalized Voronoi Graph (GVG) derived from obstacle geometry, combined with a fixed-yaw motion policy $\boldsymbol{\psi(\tau) = \mathbf{arctan2}(y(\tau), x(\tau)) - (1-\tau)\psi_s - \tau\psi_g + \pi}$ with $\boldsymbol{\tau \in [0,1]}$, from the start yaw $\boldsymbol{\psi_s}$ and the goal yaw $\boldsymbol{\psi_g}$. The second, Occlusion MPC (OccMPC)[6] treats FoV and occlusion as soft constraints in an MPC formulation. All methods were tested with $\boldsymbol{w_x = w_y = 0.5m/s}$ and $\boldsymbol{w_\psi = 0.3rad/s}$ in a 2D setting considering only horizontal FoV.

Fig. 11 illustrates results from the proposed planner and the baseline planners. As shown in Fig. 11a, the proposed planner and GVG-based planner can generate feasible trajectories that converge to the goal. However, Fig. 11b highlights a key difference: the yaw rate generated by the GVG-based planner exceeds the specified input bounds, violating the yaw rate constraints. In contrast, the proposed planner maintains all control inputs within the safe region. This discrepancy arises because the baseline relies on a fixed yaw policy, which lacks the flexibility to adapt and ensure yaw rate safety throughout the trajectory. The OccMPC method is highly sensitive to the quality of its reference trajectory; when given only the direct goal position as reference (purple trajectory in Fig. 11a), it enters the occluded region, as local updates alone cannot recover feasibility without a well-designed initial path.

We evaluated the planner's performance under vertical FoV constraints by introducing changes in the $\boldsymbol{z}$-coordinate, with a maximum vertical velocity limit of $\boldsymbol{\overline{w}_{z,\max} = 0.2m/s}$. The results are presented in Fig. 12, where it shows the top-down view of the camera trajectory, and displays the corresponding constraint violation values over time. Violations were computed for the horizontal FoV, and vertical FoV constraints. For both horizontal and vertical FoV constraints, the violation metric reflects the maximum amount by which the respective bounds were exceeded. As shown, all violation values remain non-positive throughout the trajectory, indicating that all constraints were consistently satisfied and the trajectory remained feasible.

Furthermore, Fig. 13 illustrates the application of the proposed planner in a scenario involving two PoIs. In this case, the planner successfully satisfied both horizontal FoV and occlusion constraints for all tested initial poses. The overall visibility region was computed as the intersection of the individual visibility regions corresponding to each PoI. To enforce horizontal FoV constraints effectively, a virtual

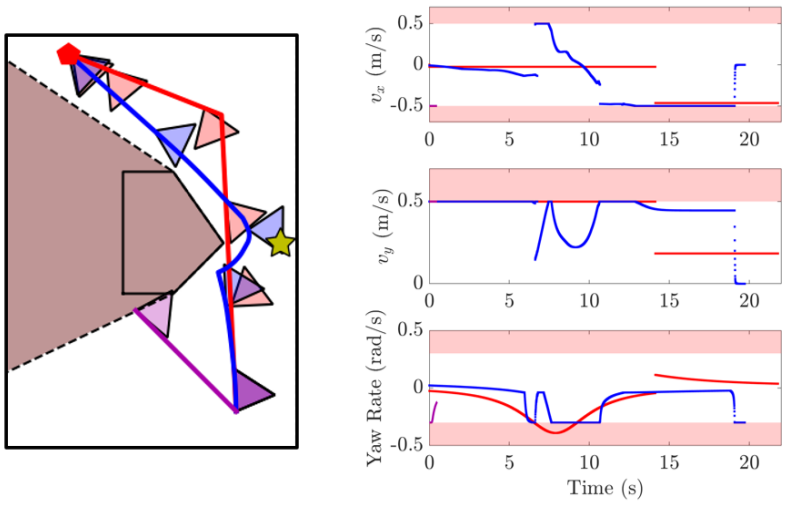

Fig. 11. Comparison of the proposed method with the baselines in a 2D environment. (Left) GVG-based planner (red) and the proposed method (blue) and OccMPC (purple) trajectories are drawn with occluded region (brown). (Right) Velocity profiles for each coordinate over time.

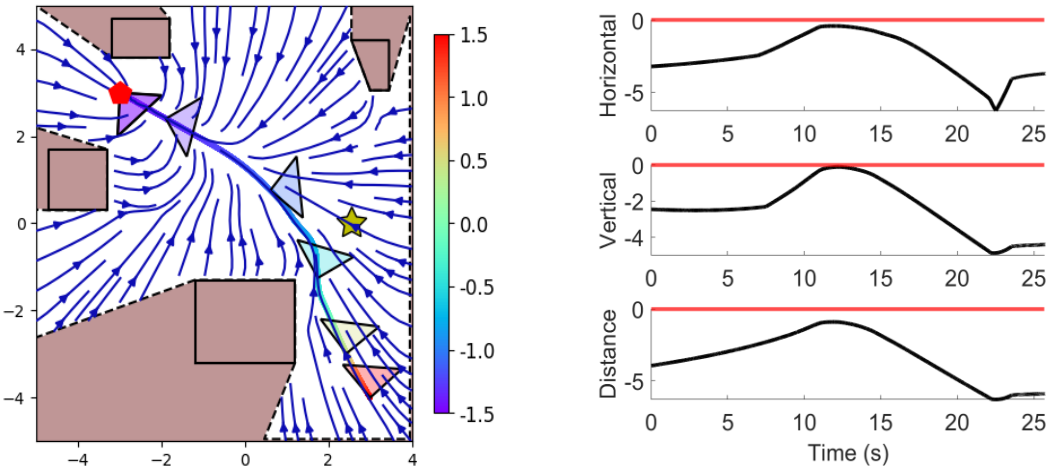

Fig. 12. (Left) Example for 4D motion planner. The z coordinate is depicted in colormap of the trajectory. (Right) The maximum violation of the horizontal/vertical FoV (Eq. (3), (5)) and distance–to–obstacle constraints (Eq. (6)), which remain non–positive throughout.

obstacle was introduced.

Hardware Experiments

We validate the proposed visibility–constrained planning method on a real quadrotor platform. Exploiting the differential flatness of quadrotor dynamics with flat outputs (x, y, z, ψ)[24], the planner generates reference trajectories for position and yaw, which are tracked by onboard controllers. This setup demonstrates applicability to real–world scenarios where visibility must be maintained. The hardware setup, shown in Fig. 1, uses a Crazyflie 2.1 quadrotor[32] equipped with an AI deck containing a front–facing grayscale camera and Wi–Fi module for transmitting images at approximately 7–8 Hz to a ground station. The ground station runs the proposed planner on a pre–built map to generate position, yaw, and velocity references, which are sent to the quadrotor via radio communication. A motion capture system provides pose estimates, and AprilTags[33] are used as PoIs for robust and reliable detection.

In the first scenario, the quadrotor navigates through four waypoints while maintaining visibility of at least one of three PoIs throughout the flight. Each trajectory segment is associated with a specific PoI,

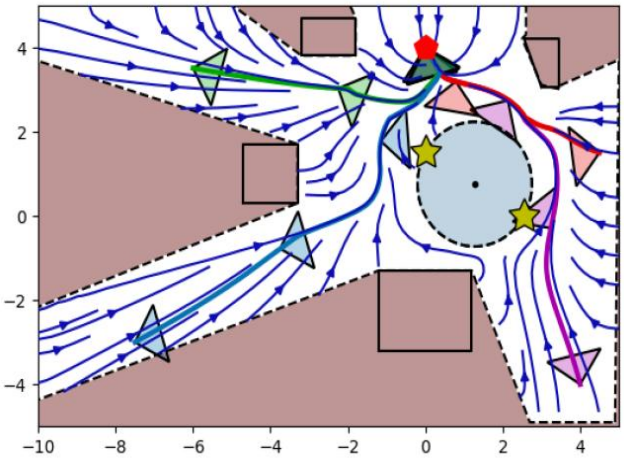

Fig. 13. Illustration of the proposed planner for two PoIs (yellow stars) with a single goal (red marker) and varying initial poses with the corresponding trajectories. The planner identifies and avoids occluded region and a virtual obstacle representing the inadmissible region.

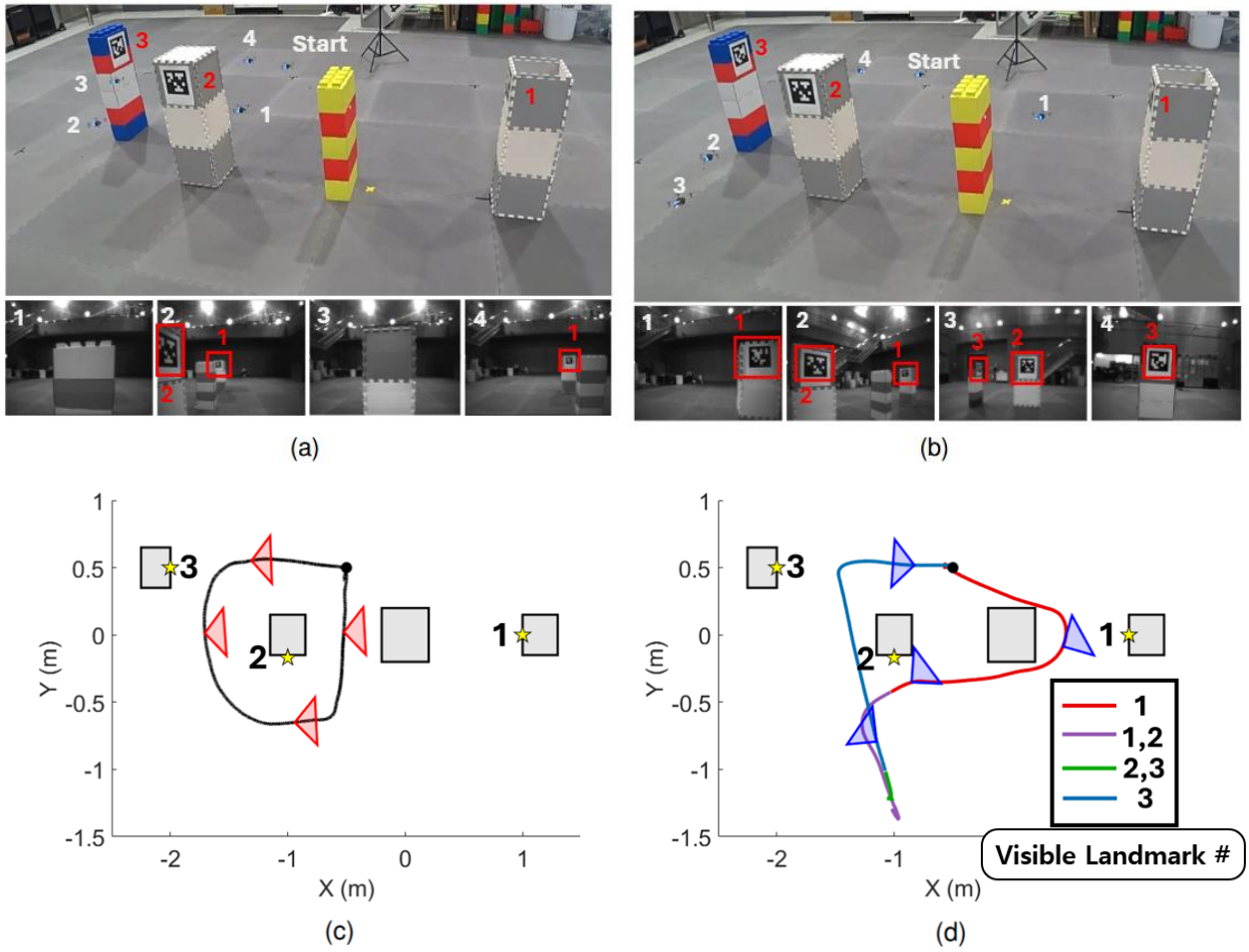

Fig. 14. Experimental results for Scenario 1. (a,c) Trajectory following waypoints without considering visibility constraints, resulting in violations caused by occlusions and limited FoV, while following the shortest path through the waypoints. (b,d) The proposed planner dynamically adjusts the trajectory by refining waypoints according to changing PoIs, ensuring visibility of at least one PoI.

and the planner must switch the PoI mid-mission when both the current and next PoIs are simultaneously visible. The baseline planner, which computes the shortest path without considering visibility constraints, frequently violates the visibility requirement due to occlusions in the first segment and horizontal FoV limitations in later segments. In contrast, the proposed pla nner modifies the path and introduces intermediate waypoints when necessary to ensure that visibility is always maintained. For instance, it adjusts the first segment so that both the first and second PoIs remain visible during the transition, avoids occlusions of PoI 1, and switches the tracked PoI at moments when both are within view. This process is repeated for subsequent waypoints until the goal is reached. Onboard images shown in Fig. 14 confirm that the proposed method maintains visibility of at least one PoI at every time step, whereas the baseline does not.

The second scenario evaluates the enforcement of vertical FoV constraints by positioning four PoIs at different heights around the flight area in a rectangular trajectory. Here, the baseline planner enforces only horizontal FoV constraints as in Eq. (13), while the proposed planner applies the full formulation in Eq. (23) to enforce both horizontal and vertical FoV limits. Although the baseline planner successfully keeps the PoIs within the horizontal FoV, it fails to maintain them within the vertical FoV, particularly when the quadrotor is closest to the PoIs, resulting in partial or complete loss of visibility. In contrast, the proposed planner adjusts the z-coordinate jointly with the other coordinates, ascending when the PoI is above the quadrotor and descending when it is below, thereby ensuring full FoV compliance.

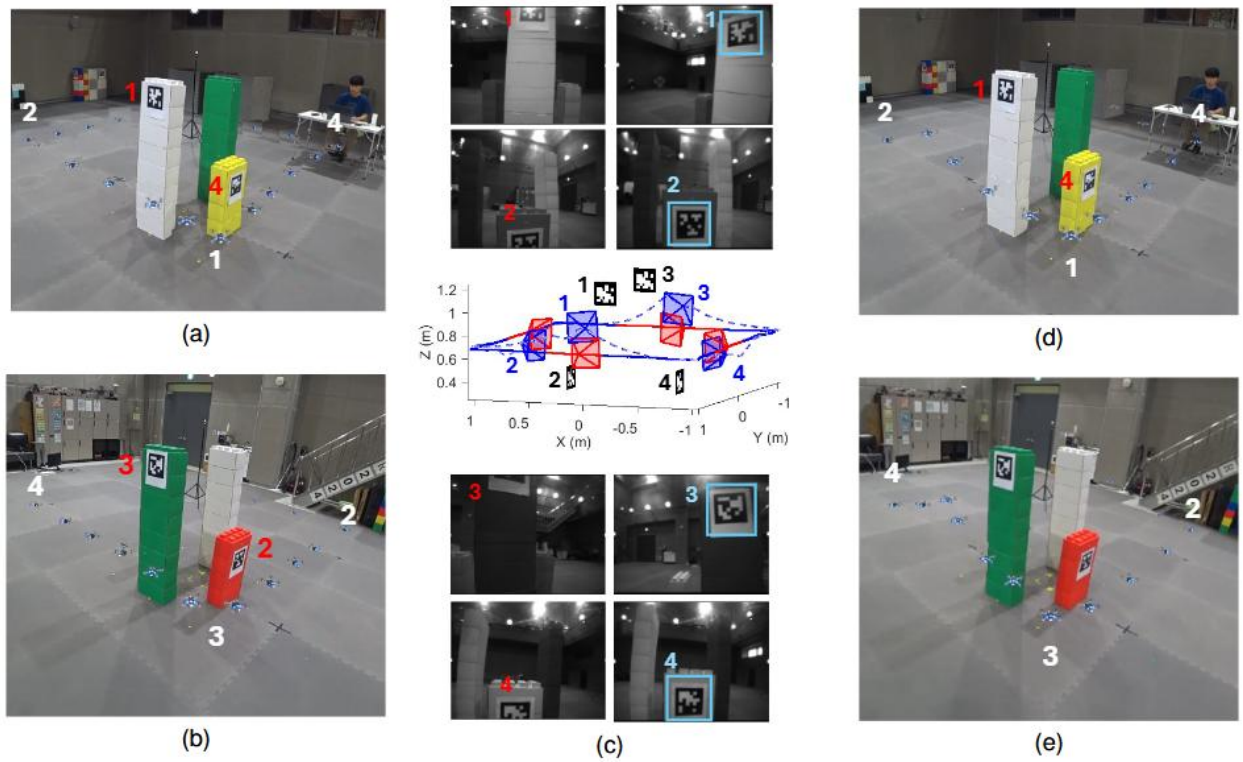

Fig. 15. Experimental results for Scenario 2. (a–b) The baseline algorithm considers only horizontal FoV constraints during waypoint traversal. (d–e) The proposed planner incorporates full FoV constraints, generating modified vertical trajectories to maintain visibility within the limited vertical FoV. (c) First-person-view images at moments when vertical FoV constraints are at risk of being violated; baseline on the left, proposed planner on the right. Trajectories for the proposed planner (dashed line) and the baseline planner (solid line) are visualized, with infeasible instances highlighted in red.

Onboard images in Fig. 15 confirm that the PoIs remain fully visible even at the closest approach points, where FoV violations would otherwise occur.

Conclusion

This article presented a planning and control pipeline for visibility-constrained flight of micro aerial vehicles that avoids optimization, making it well-suited for resource-limited platforms. The proposed control framework maintains visibility of designated points of interest (PoIs) under limited field-of-view and environmental occlusion constraints, while guaranteeing convergence to the goal despite the highly nonconvex nature of the visibility constraints. The framework was further extended to handle multiple PoIs, enabling flexible visibility management in complex tasks. Simulation results with both single and multiple PoIs show that, compared to soft-constraint approaches such as model predictive control, the method consistently produces admissible, converging trajectories with only a fraction of the computational cost. The approach was also validated on a quadrotor platform as a reference trajectory generator, confirming its applicability to real-world vision-based localization and navigation scenarios.

Future work will extend the current first-order kinematic control formulation to higher-order dynamic systems, incorporate time-varying occlusion constraints from dynamic obstacles, and generalize the current attitude constraints to the full $SO(3)$ space, enabling application to more complex and realistic operational settings.

Appendix

Proof of Theorem 1 (Feasibility & Convergence)

Setup and Notation:

Let $\mathbf{y} = (x, y, z, \psi)^T \in \mathcal{C}$. The admissible set is

$$\mathcal{A} = \mathcal{A}_{h,FoV} \cap \mathcal{A}_{v,FoV} \cap \mathcal{A}_{occ}$$

where $\mathcal{A}_{h,FoV}$ is the admissible set according to the FoV constraints Eqs. (3), (5), and $\mathcal{A}_{v,FoV}$ is with the constraint Eq. (4), and $\mathcal{A}_{occ}$ is with the occlusion constraint Eq. (6).

The control law is the CVF in (23): it combines (i) the horizontal FoV mechanism of (13) built from the diffeomorphism φ and barrier P_r (Eqs. (10)–(12)), (ii) the vertical coordination of (18)–(19), and (iii) the occlusion-aware planar modulation (22). Gains $Hq, H \succ 0$ and the normalization $\eta > 0$ enforce input bounds and do not affect the sign of descent arguments.

We assume: (a) $\mathcal{A} \neq \emptyset$, (b) $\mathbf{y}_g \in \mathrm{int}(\mathcal{A})$, (c) the standard regularity of the boundaries (locally $\mathcal{C}^1$) and Lipschitz vector fields away from switching surfaces, and (d) the small parameters in (16) satisfy $0 < \epsilon_z < \delta \ll 1$.

Step 1: Forward invariance of each constraint class

(i) Horizontal FoV invariance (constraints (3),(5))

In the horizontal state $\mathbf{y}_q = (x, y, \psi)^T$, the map $\varphi: \mathcal{A}_S \to Q = \mathrm{int}\,(\mathcal{A}_{S,p}) \times [0,1]$ sends the nonconvex yaw-admissible set to a convex strip Q in the transformed yaw coordinate $\xi \in [0,1]$. Define the horizontal potential

$$P_h(y_q) = \frac{k}{2}\left\|\varphi(y_q) - \varphi(y_{g,q})\right\|^2 + P_r(\xi),$$

with P_r the barrier of Eq. (11). The CVF (13) implements a preconditioned negative gradient of P_h (pulled back through $\nabla\varphi$):

$$\dot{y}_q = -\frac{1}{\eta} H_q (\nabla\varphi)^{-1} \nabla P_h.$$

Hence

$$\dot{P}_h = \nabla P_h^T \dot{y}_q = -\frac{1}{\eta}\|\nabla P_h\|_{H_q}^2 \leq 0.$$

As $\xi \to 0$ or $\xi \to 1$ we have $P_r(\xi) \to \infty$, so the boundary $\xi \in \{0,1\}$ is an infinite-energy barrier and cannot be crossed from finite P_h. Equivalently, the Neumann boundary condition holds: at $\xi = 0$ (resp. $\xi = 1$) the normal component of the flow is non-outward, so (3), (5) are forward invariant.

(ii) Vertical FoV invariance (constraints (4))

Let $\overline{z}(x, y, \psi)$, $\underline{z}(x, y, \psi)$ be the vertical bounds and define the safety margins $m_z^+ = \overline{z} - z$, $m_z^- = z - \underline{z}$. The hybrid direction $\mathbf{g}_u$ (18) uses:

- Interior mode $\mathbf{d}_d$: move toward z_g (Eq. (14)); trivially keeps $m_z^+, m_z^- > 0$.
- Boundary-active modes $\overline{\mathbf{d}}_m, \underline{\mathbf{d}}_m$: replace the vertical component by the directional derivatives $D_{\mathbf{g}_q}\overline{z}$ or$D_{\mathbf{g}_q}\underline{z}$, which, by construction, do not decrease the active safety margin ($\dot{m}_z^+ \geq 0$ on $\overline{z} = z$, $\dot{m}_z^- \geq 0$ on $\underline{z} = z$).
- Narrow-tube mode $\mathbf{d}_z$: when $z = z^l$ and both margins are below δ but above ϵ_z, the controller holds altitude ($\dot{z} = 0$), preserving feasibility.

Thus $m_z^+, m_z^- \geq 0$ for all t, i.e., (4) is forward invariant.

(iii) Occlusion invariance

For a fixed PoI $\mathbf{p}^l$, the occlusion-free set $S(\mathbf{p}^l, O)$ is (strictly) star-shaped with $\mathbf{p}^l$ in its kernel (definition of visibility segments). The planar modulation in (22) yields

$$\dot{\mathbf{y}}_p = N(\mathbf{y}_p, S) f_{a,p}(\mathbf{y}_p, \mathbf{y}_{g,p}),$$

where $N(\mathbf{y}_p, S)$ is chosen so that on ∂S the normal component of $\dot{\mathbf{y}}_p$ is non-outward (a Neumann-type condition) and in the interior N is positive definite. Consequently, if $\mathbf{y}_p(0) \in \mathrm{int}(S)$ then $\mathbf{y}_p(t) \in \mathrm{int}(S)$ for all $t \geq 0$.

(iv) Forward invariance of $\mathcal{A}$

The mechanisms above act on complementary coordinates and are composed in Eq. (23) by a block structure:

- the diffeomorphism/barrier acts only through φ (via ξ);
- the planar modulation acts only on $\mathbf{y}_p = (x, y)$;
- the vertical logic acts only on z.

Therefore, no mechanism breaks the invariance established by another, and the intersection $\mathcal{A}$ is forward invariant.

Step 2: Convergence to the goal within $\mathcal{A}$

Consider the composite Lyapunov candidate

$$V(\mathbf{y}) = \frac{1}{2}\left\|\varphi(\mathbf{y}_q) - \varphi(\mathbf{y}_{g,q})\right\|^2 + P_r(\xi) + \frac{1}{2}\left\|y_p - y_{g,p}\right\|^2 + \frac{1}{2}(z - z_g)^2.$$

All three terms are nonnegative and V=0V=0 only at y=ygy=yg. Along solutions of (23):

- Horizontal term. As above, $V_h = 1/2\left\|\varphi(\mathbf{y}_q) - \varphi(\mathbf{y}_{g,q})\right\|^2 + P_r(\xi)$,

$$\dot{V}_h = -\frac{1}{\eta}\|\nabla V_h\|^2_{H_q} \leq 0,$$

with $\dot{V}_h = 0$ iff $\varphi(\mathbf{y}_q) = \varphi(\mathbf{y}_{g,q})$ and the repulsive component vanishes (interior).

- Planar (Occlusion-aware) term. Inside $\mathrm{int}(S)$, $N(\mathbf{y}_p, S) \succ 0$ and

$$\dot{V}_P = \nabla V_P^T \dot{\mathbf{y}}_P = (\mathbf{y}_p - \mathbf{y}_{g,p})^T N(\mathbf{y}_P, S) f_{a,.p} = -\frac{1}{\eta}\left\|N^{\frac{1}{2}}(\mathbf{y}_p, S)\nabla V_P\right\|^2 \leq 0.$$

On $\partial S, N$ removes outward components, so $\dot{V}_P \leq 0$ with equality only if the tangential attraction is zero (i.e. $\mathbf{y}_p = \mathbf{y}_{g,p}$ projected in S).

- Vertical term (hybrid):

Interior mode $\mathbf{d}_d$: $\dot{V}_z = -(z - z_g)^2/\eta \leq 0$ with equality only at $z = z_g$.

Boundary-active modes : the vertical component aligns with $D_{g_q}\overline{z}$ or $D_{g_q}\underline{z}$, which maintains feasibility; V_z is non-increasing (may be constant while sliding along the boundary).

Narrow-tube mode: $\dot{V}_z = 0$ but $V_h + V_P$ continues decreasing unless already at the horizontal goal.

Combining, $\dot{V} \leq 0$ for all modes (and across mode switches, since (19) only normalizes the vector field). V is radially unbounded on $\mathcal{A}$ and bounded below by 0. By LaSalle's invariance principle[34], trajectories approach the largest weakly invariant set contained in $\{\dot{V} = 0\}$. The equalities above require simultaneously:

$$\varphi(\mathbf{y}_q) = \varphi(\mathbf{y}_{g,q}),\ \mathbf{y}_p = \mathbf{y}_{g,p}\ (\text{in } S),\ z = z_g,$$

i.e., $\mathbf{y} = \mathbf{y}_g$. Therefore $\mathbf{y}(t) \to \mathbf{y}_g$ as $t \to \infty$ while $y(t) \in \mathcal{A}$ for all t, proving convergence.

References

[1] J. Lin, Y. Wang, Z. Miao, H. Wang, and R. Fierro, “Robust image-based landing control of a quadrotor on an unpredictable moving vehicle using circle features,” IEEE Transactions on Automation Science and Engineering, vol. 20, no. 2, pp. 1429–1440, Apr. 2022.

[2] J. Mao, S. Nogar, C. M. Kroninger, and G. Loianno, “Robust active visual perching with quadrotors on inclined surfaces,” IEEE Trans. on Robotics, vol. 39, no. 3, pp. 1836–1852, Feb. 2023.

[3] J. Xing, G. Cioffi, J. Hidalgo-Carrió, and D. Scaramuzza, “Autonomous power line inspection with drones via perception-aware mpc,” in 2023 IEEE/RSJ International Conference on Intelligent Robots and Systems (IROS), pp. 1086–1093, Oct. 2023.

[4] M. Jacquet and A. Franchi, “Motor and perception constrained nmpc for torque-controlled generic aerial vehicles,” IEEE Robotics and Automation Letters, vol. 6, no. 2, pp. 518–525, Apr. 2020.

[5] D. Falanga, P. Foehn, P. Lu, and D. Scaramuzza, “Pampc: Perception-aware model predictive control for quadrotors,” in 2018 IEEE/RSJ International Conference on Intelligent Robots and Systems (IROS), pp. 1086–1093, Oct. 2018.

[6] G. Allibert, E. Courtial, and F. Chaumette, “Predictive control for constrained image-based visual servoing,” IEEE Trans. on Robotics, vol. 26, no. 5, pp. 933–939, Oct. 2010.

[7] K. Zhang, Y. Shi, and H. Sheng, “Robust nonlinear model predictive control based visual servoing of quadrotor uavs,” IEEE/ASME Trans. on Mechatronics, vol. 26, no. 2, pp. 700–708, Apr. 2021.

[8] I. Ibrahim, F. Farshidian, J. Preisig, P. Franklin, P. Rocco, and M. Hutter, “Whole-body mpc and dynamic occlusion avoidance: A maximum likelihood visibility approach,” in 2022 International Conference on Robotics and Automation (ICRA), pp. 221–227, May 2022.

[9] D. Nicolis, M. Palumbo, A. M. Zanchettin, and P. Rocco, “Occlusion-free visual servoing for the shared autonomy teleoperation of dual-arm robots,” IEEE Robotics and Automation Letters, vol. 3, no. 2, pp. 796–803, Apr. 2018.

[10] I. Salehi, G. Rotithor, R. Saltus, and A. P. Dani, “Constrained image-based visual servoing using barrier functions,” in 2021 IEEE International Conference on Robotics and Automation (ICRA), pp. 14254–14260, May 2021.

[11] B. Trimarchi, F. Schiano, and R. Tron, “A control barrier function candidate for limited field of view sensors,” arXiv preprint arXiv:2410.01277, 2024.

[12] S. Wei, B. Dai, R. Khorrambakht, P. Krishnamurthy, and F. Khorrami, “Diffocclusion: Differentiable optimization based control barrier functions for occlusion-free visual servoing,” IEEE Robotics and Automation Letters, vol. 9, no. 4, pp. 3235–3242, Apr. 2024.

[13] S. Bhattacharya, R. Murrieta-Cid, and S. Hutchinson, “Optimal paths for landmark-based navigation by differential-drive vehicles with field-of-view constraints,” IEEE Trans. on Robotics, vol. 23, no. 1, pp. 47–59, Feb. 2007.

[14] I. Spasojevic, V. Murali, and S. Karaman, “Perception-aware time optimal path parameterization for quadrotors,” in 2020 IEEE International Conference on Robotics and Automation (ICRA), pp. 3213–3219, May 2020.

[15] R. Zou and S. Bhattacharya, “On optimal pursuit trajectories for visibility-based target-tracking game,” IEEE Trans. on Robotics, vol. 35, no. 2, pp. 449–465, Dec. 2018.

[16] E. Rimon, Exact robot navigation using artificial potential functions. Yale University, New Haven, 1990.

[17] S. M. LaValle, Planning algorithms. Cambridge university press, Cambridge, 2006.

[18] O. Khatib, “Real-time obstacle avoidance for manipulators and mobile robots,” The international journal of robotics research, vol. 5, no. 1, pp. 90–98, Mar. 1986.

[19] C. I. Connolly and R. A. Grupen, “The applications of harmonic functions to robotics,” Journal of robotic Systems, vol. 10, no. 7, pp. 931–946, Oct. 1993.

[20] O. Arslan and D. E. Koditschek, “Sensor-based reactive navigation in unknown convex sphere worlds,” The International Journal of Robotics Research, vol. 38, no. 2-3, pp. 196–223, Mar. 2019.

[21] S. G. Loizou and E. D. Rimon, “Mobile robot navigation functions tuned by sensor readings in partially known environments,” IEEE Robotics and Automation Letters, vol. 7, no. 2, pp. 3803–3810, Apr. 2022.

[22] L. Huber, J.-J. Slotine, and A. Billard, “Avoiding dense and dynamic obstacles in enclosed spaces: Application to moving in crowds,” IEEE Transactions on Robotics, vol. 38, no. 5, pp. 3113–3132, Oct. 2022.

[23] V. Vasilopoulos, G. Pavlakos, K. Schmeckpeper, K. Daniilidis, and D. E. Koditschek, “Reactive navigation in partially familiar planar environments using semantic perceptual feedback,” The International Journal of Robotics Research, vol. 41, no. 1, pp. 85–126, Jan. 2022.

[24] D. Kim, M. Pezzutto, L. Schenato, and H. J. Kim, “Visibility-constrained control of multirotor via reference governor,” in 62th IEEE conference on decision and control (CDC), pp. 5714–5721, Dec. 2023.

[25] D. Mellinger and V. Kumar, "Minimum snap trajectory generation and control for quadrotors," in 2011 IEEE international conference on robotics and automation (ICRA), pp. 2520–2525, May. 2011.

[26] A. Cotorruelo, D. R. Ramirez, D. Limon, and E. Garone, “Nonlinear mpc for tracking for a class of nonconvex admissible output sets,” IEEE Transactions on Automatic Control, vol. 66, no. 8, pp. 3726–3732, Aug. 2021.

[27] L. Huber, A. Billard, and J.-J. Slotine, “Avoidance of convex and concave obstacles with convergence ensured through contraction,” IEEE Robotics and Automation Letters, vol. 4, no. 2, pp. 1462–1469, Apr. 2019.

[28] K. J. Obermeyer and Contributors, “VisiLibity: A C++ library for visibility computations in planar polygonal environments,” http://www.VisiLibity.org, 2008, v1.

[29] J. Mikula and M. Kulich, “TřiVis: Versatile, Reliable, and High-Performance Tool for Computing Visibility in Polygonal Environments,” in 2024 IEEE/RSJ International Conference on Intelligent Robots and Systems (IROS), pp. 10503–10510, Oct. 2024.

[30] A. Dahlin and Y. Karayiannidis, “Creating star worlds: Reshaping the robot workspace for online motion planning,” IEEE Transactions on Robotics, vol. 39, no. 5, pp. 3655–3670, Oct. 2023.

[31] J.-B. Hayet, H. Carlos, C. Esteves, and R. Murrieta-Cid, “Motion planning for maintaining landmarks visibility with a differential drive robot,” Robotics and Autonomous Systems, vol. 62, no. 4, pp. 456–473, Apr. 2014.

[32] Bitcraze, “Crazyflie 2.1,” https://www.bitcraze.io/products/crazyflie-2-1/, 2023, [Online; accessed Jul. 11, 2024].

[33] E. Olson, “Apriltag: A robust and flexible visual fiducial system,” in 2011 IEEE international conference on robotics and automation (ICRA), pp. 3400–3407, May 2011.

[34] R. Goebel, R. G. Sanfelice, and A. R. Teel, “Hybrid dynamical systems,” IEEE control systems magazine, vol. 29, no. 2, pp. 28–93, Apr. 2009.